

## PROGRESS WITH LUMINESCENCE IMAGING FOR THE CHARACTERISATION OF SILICON WAFERS AND SOLAR CELLS

T. Trupke<sup>1</sup>, R.A. Bardos<sup>1</sup>, M.D. Abbott<sup>1</sup>, P. Würfel<sup>2</sup>, E. Pink<sup>1</sup>, Y. Augarten<sup>1</sup>, F.W. Chen<sup>1</sup>, K. Fisher<sup>1</sup>, J.E. Cotter<sup>1</sup>, M. Kasemann<sup>3</sup>, M. Rüdiger<sup>3</sup>, S. Kontermann<sup>3</sup>, M.C. Schubert<sup>3</sup>, M. The<sup>3</sup>, S.W. Glunz<sup>3</sup>, W. Warta<sup>3</sup>, D. Macdonald<sup>4</sup>, J. Tan<sup>4</sup>, A. Cuevas<sup>4</sup>, J. Bauer<sup>5</sup>, R. Gupta<sup>5</sup>, O. Breitenstein<sup>5</sup>, T. Buonassisi<sup>6</sup>, G. Tarnowski<sup>6</sup>, A. Lorenz<sup>6</sup>, H.P. Hartmann<sup>7</sup>, D.H. Neuhaus<sup>7</sup>, J.M. Fernandez<sup>8</sup>

<sup>1</sup>Centre of Excellence for Advanced Silicon Photovoltaics and Photonics, University of New South Wales, Sydney, 2052, NSW, Australia, Tel.: +61 2 9385 4054, Fax: +61 2 9662 4240, email: [thorsten@trupke.de](mailto:thorsten@trupke.de)

<sup>2</sup>Universität Karlsruhe, Karlsruhe, Germany

<sup>3</sup>Fraunhofer Institute for Solar Energy Systems (ISE), Freiburg, Germany

<sup>4</sup>The Australian National University, Canberra, Australia

<sup>5</sup>Max Planck Insitut für Mikrostrukturphysik, Halle, Germany

<sup>6</sup>Evergreen Solar Inc., Marlboro, USA

<sup>7</sup>Deutsche Cell GmbH, Freiberg, Germany

<sup>8</sup>BP Solar, Tres Cantos, Spain

**ABSTRACT:** Electroluminescence (EL) and photoluminescence (PL) imaging have recently been demonstrated to be fast experimental techniques that allow measurement of the spatial distribution of the diffusion length in silicon solar cells and of the minority carrier lifetime in large area silicon wafers [1, 2]. A practical advantage of these techniques is that data acquisition times for high resolution luminescence images are typically on the order of only one second. This paper reviews previous work related to process monitoring by luminescence imaging techniques and discusses some recent progress in the areas of several experimental and theoretical aspects of luminescence imaging. It is shown that luminescence imaging is an exceptionally versatile tool that provides spatially resolved information about a variety of material and solar cell parameters with data acquisition times that are compatible with in-line process monitoring.

**Keywords:** Silicon, Characterisation, Photoluminescence

### 1 INTRODUCTION

Bulk crystalline silicon is an indirect band gap material and as such is generally a relatively poor light emitter due to the fact that phonons are involved in optical transitions. External PL quantum efficiencies on the order of several percent can be achieved in very pure silicon wafers with excellent surface passivation [3]. External EL quantum efficiency of PERL solar cells on the order of one percent have also been demonstrated, when the cells were used as silicon light emitting diodes [4]. However, in silicon wafers that are typically used in industrial photovoltaic applications, luminescence quantum efficiencies are on the order  $10^{-6}$ . The demonstration of quasi steady state photoluminescence (QSS-PL) as a very sensitive experimental method to determine the injection level dependent minority carrier lifetime in silicon wafers [5] therefore came as a surprise.

Spatially resolved PL mapping measurements have been used in Photovoltaics (PV) research for some time [6-8] and the general benefits of using luminescence as a characterisation tool for silicon solar cells have also been pointed out previously by various authors (e.g. [9-12]). An important recent development in terms of a practical implementation of luminescence characterisation has been the demonstration of luminescence imaging techniques for large area silicon solar cells and silicon wafers typically used in PV. EL imaging, in which a forward bias is applied to a finished solar cell in the dark, was introduced on mc-Si solar cells by T. Fuyuki et. al and proposed as a technique to measure the spatially resolved diffusion length [1]. PL imaging, where the

emission of light is stimulated by external illumination, was introduced soon afterwards [2]. Compared to EL imaging PL is advantageous as it is applicable to silicon wafers at any processing stage. In both EL and PL imaging silicon CCD cameras were used for the detection. The luminescence distribution of the entire sample is captured with the acquisition of a single CCD camera image, which makes luminescence imaging exceptionally fast.

Since the introduction of EL and PL imaging a variety of specialised applications for luminescence imaging on large area silicon devices and wafers have been developed which shall be reviewed in this paper. Note that most images will appear with somewhat reduced image quality in this paper. A high quality pdf-version of the paper is available upon request from the corresponding author.

### 2 MINORITY CARRIER LIFETIME IMAGING

PL imaging is an exceptionally fast experimental method for spatially resolved measurement of the effective minority carrier lifetime  $\tau_{\text{eff}}$ . General benefits of quasi steady state PL lifetime measurements include the robustness of steady state or quasi steady state PL measurements against experimental artefacts occurring in other techniques at low to moderate injection densities. These artefacts can result from minority carrier trapping [13] or from excess carriers stored in space charge regions [5], the latter causing the so-called depletion

region modulation effect [14, 15]. Neglecting photon reabsorption within the silicon wafer [16], and assuming low injection conditions the local luminescence intensity is given by the average excess minority carrier density  $\Delta n$  across the thickness of the wafer

$$I_{PL} = C \cdot N_{D/A} \cdot \frac{1}{d} \cdot \int_0^d \Delta n(x) dx = C \cdot N_{D/A} \cdot \Delta n \quad (1)$$

where  $N_{D/A}$  is the doping concentration  $\Delta n(x)$  is the local minority carrier concentration and  $d$  is the thickness of the sample. Since PL imaging is carried out under steady state conditions, the minority carrier lifetime is given as

$$\tau_{eff} = \frac{\Delta n}{G} \quad (2)$$

where  $G$  is the average minority carrier generation rate per volume. The determination of the calibration constant  $C$  in Eq.1 is crucial for quantitative lifetime measurements, and is a more challenging task in QSS-PL than in other techniques such as quasi steady state photoconductance (QSS-PC) [17]. This is mainly because the calibration constant varies from one wafer to the next due to optical effects.

The first absolute minority carrier lifetime distribution from a PL image was presented in [2] for a passivated mc-Si wafer. In the same reference good quantitative agreement with Carrier Density Imaging [18] was demonstrated. Fig.1b shows a calibrated PL image of a p-type string ribbon wafer after phosphorous diffusion plus SiN deposition and firing. The colour bar gives the effective minority carrier lifetime in  $\mu s$ . For comparison Fig.1a shows a lifetime *map* taken on the same wafer with a commercial ( $\mu$ -PCD) microwave photoconductance decay ( $\mu$ -PCD) tool.

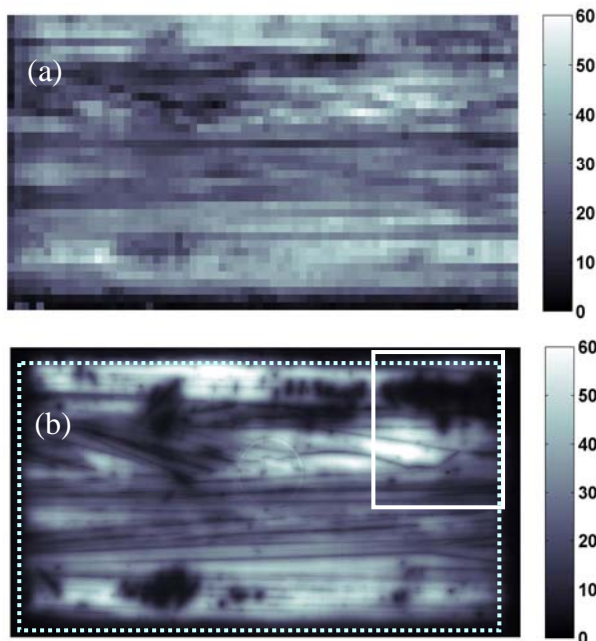


**Figure 1:** Effective Minority carrier lifetime in  $\mu s$  measured on a  $8 \times 15 \text{ cm}^2$  string ribbon wafer after emitter diffusion and SiN firing. (a)  $\mu$ -PCD map measured in 100 s with 2 mm per pixel spatial resolution. (b) PL image measured in 1 s with  $160 \mu m$  per pixel

Note that the  $\mu$ -PCD tool measured only the part of the wafer that is highlighted in the PL image with a dotted line, whereas the PL image represents the actual wafer area including the edge region with very low ( $<5\mu s$ ) lifetime. Good quantitative agreement between the two independently calibrated measurements is observed over most of the wafer area. The calibration of the PL image was achieved by comparison with a spatially averaged QSS-PC measurement. The PL image was measured with a total data acquisition time of only one second and with a spatial resolution of  $160 \times 160 \mu m^2$  per pixel. For comparison, the  $\mu$ -PCD measurement took 100s with a significantly poorer spatial resolution of  $2 \times 2 \text{ mm}^2$  per pixel. While good quantitative agreement is observed over most of the wafer area, the PL image reveals various blurry patches of strongly reduced intensity which are not as clearly identified in the  $\mu$ -PCD measurement (e.g. white square).

The PL image in Fig.1b was taken with one-Sun equivalent illumination intensity. Fig.2 shows a PL image of the blurry region marked in Fig.1b with a white square taken with ten-Suns equivalent illumination intensity. That image reveals that the origin of the low carrier density regions in the PL image from Fig.1b are caused by very small localised defects that are too small to be detected reliably in the relatively crude  $\mu$ -PCD map. The blurring around these features that is observed in the PL image measured with one-Sun equivalent illumination is caused by lateral currents flowing from adjacent high lifetime regions into the defected region and is especially pronounced because an emitter has already been formed on the wafer. To obtain the minority carrier lifetime from the image in Fig.1b, these lateral currents would have to be accounted for numerically as has been discussed previously in relation to the CDI technique [19].

The reason for the reduced blurring in the area surrounding local recombination sites in PL images measured with higher illumination intensity (Fig.2) is that at higher illumination intensity the lateral currents flowing into the defected region become larger. The series resistance of the emitter then more effectively isolates these regions from the surrounding high lifetime regions, i.e. voltage drops occur over shorter distances. Using two dimensional network modelling to describe quantitatively the influence of local shunts or recombination active sites on luminescence will be helpful to describe these blurring effects more quantitatively [20]. Experimental results on PL images carried out with variable light intensities combined with such modelling will help developing methods to distinguish shunts from other recombination active areas.

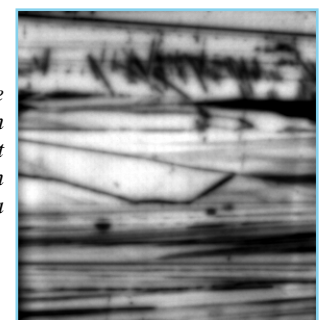


**Figure 2:** PL image measured in 1 s and with ten-Suns equivalent illumination intensity on the area marked with a white square in Fig.1.

PL imaging at different light intensities thus offers the flexibility of measuring the effect of a defect on the lateral carrier density under realistic operating conditions (Fig.1b) and accurately localising the defects at a higher illumination intensity (Fig.2).

The PL image taken at ten-Suns gives the minority carrier lifetime with only minor influence of lateral smearing, however at an injection level that is exceeding the normal operating conditions of the solar cell. It should be noted, however, that the  $\mu$ -PCD tool uses intensities equivalent to hundreds of Suns, thereby providing lifetimes at injection conditions that are even further from the operating conditions of the solar cell. The reason for the quantitative agreement between the PL image and the  $\mu$ -PCD measurement in Fig.1 is that according to an injection level dependent QSS-PL lifetime measurement (not shown here) the injection level dependence of the minority carrier lifetime in this wafer is weak, varying by only 20% over two orders of magnitude of illumination intensity.

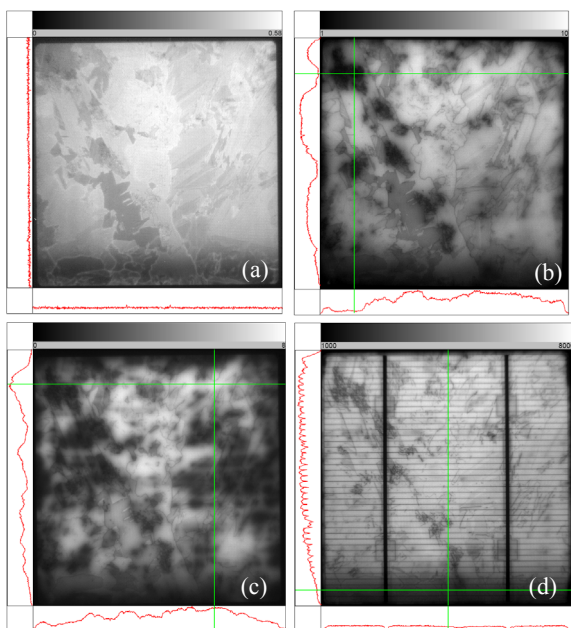


**Figure 3:** Effective Minority carrier lifetime in  $\mu$ s from PL images measured on 5-inch mc-Si sister wafers after (a) surface damage etch, (b) emitter diffusion, (c) SiN deposition (not fired), (d) fully processed cell [color scale in counts per pixel and second for (d)].

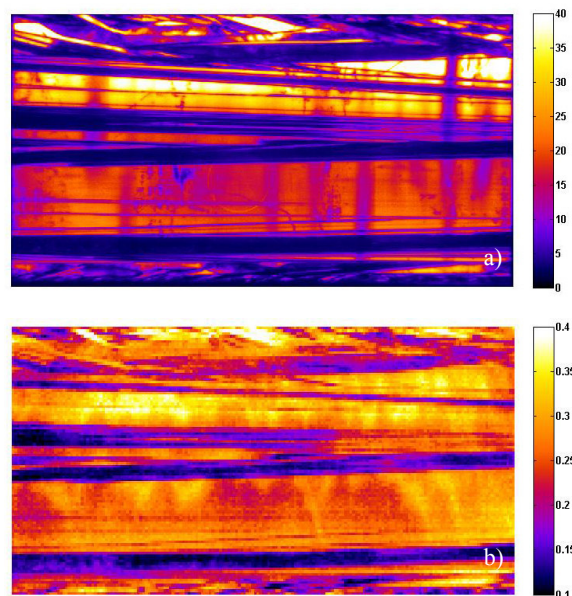
### 2.1 Process monitoring

Fig.3 shows calibrated PL images of various neighbouring mc-Si sister wafers at different processing stages: after NaOH etch (a), after emitter diffusion (b), after SiN deposition (c) and fully processed cell (d). Each image in Fig.3 taken with only one to ten seconds (3a) data acquisition time each. A further reduction of the data acquisition time can be achieved e.g. via 3x3 binning of pixels, thereby sacrificing spatial resolution. The images shown in Fig.3 highlight the possibility of monitoring the influence of individual processing steps on the local material parameters in an in-line process. For example the image taken on the as-cut wafer and all subsequent images show an area of reduced lifetime near the bottom

edge. That area is still visible in the image taken on the finished cell. This low lifetime region near the edge of the wafer is caused by a defect rich region near the outer, bottom or top region of a cast ingot. This example shows that PL images may be used as an efficient quality control tool for raw wafers by both wafer and cell manufacturers.

The low lifetime of only  $\sim 400$ ns in the unpassivated wafer after NaOH etch (Fig.3a) results from the diffusion limitation of the carrier lifetime and agrees well with the value that is calculated for an infinite recombination velocity on both surfaces for the illumination wavelength of 815nm.

### 2.2 PL imaging in iodine solution



**Figure 4:** Effective minority carrier lifetime in  $\mu$ s measured on an as grown  $8 \times 15 \text{ cm}^2$  string ribbon wafer. (a) after HF dip and with iodine ethanol surface passivation, (b) without surface passivation.

The surface passivation of silicon wafers by immersion in HF has been shown previously to yield exceptionally low surface recombination velocities of 0.25 cm/s [21]. In mc-Si wafers immersed in HF the effective minority carrier lifetime is thus dominated by the bulk. Sugimoto and Tajima recently demonstrated the benefits of PL imaging of mc-Si wafers immersed in HF [22]. Due to the associated reduction in data acquisition time, the same group was able to measure wafers cut from different positions of a cast block, thereby providing three-dimensional information about the distribution of defects [23]. The operational health and safety issues associated with handling HF are not acceptable in many environments (e.g. in characterisation laboratories). Passivation by iodine ethanol or iodine methanol solution following HF dipping is therefore commonly used as a much safer alternative.

Calibrated PL images (colour bar gives effective lifetime in  $\mu$ s) of an as grown string ribbon wafer before and after HF dipping and iodine ethanol passivation are shown in Fig.4. The comparison of the two images shows that iodine immersion after HF dipping allows the bulk lifetime to be measured, whereas the measurement on the

raw wafer gives the diffusion limited lifetime in high bulk lifetime grains ( $\sim 400$  ns in this wafer for 815 nm illumination wavelength). The correlation between the two images in Fig.4 also shows that PL images allow areas of low bulk lifetime to be identified already in measurements on unprocessed raw wafers.

PL imaging with iodine ethanol passivation after HF dipping and rinsing is thus a safer alternative to measurements in HF solution. In practice the wafer can actually be measured without being immersed in the solution. After the HF treatment the wafers can be stored in the iodine ethanol solution for days without significant deterioration of the surface passivation. After taking the wafer out of the solution a homogeneous film is formed on both polished and rough surfaces that preserves the passivation for about two minutes, more than enough for loading the wafer into the PL imaging set-up and making the measurement.

### 3 DIFFUSION LENGTH IMAGING

Fuyuki et al proposed EL imaging as a fast technique to measure spatially resolved diffusion lengths in silicon solar cells [1]. They observed a linear relationship between the local luminescence intensity and the local diffusion length in some small area silicon solar cells.

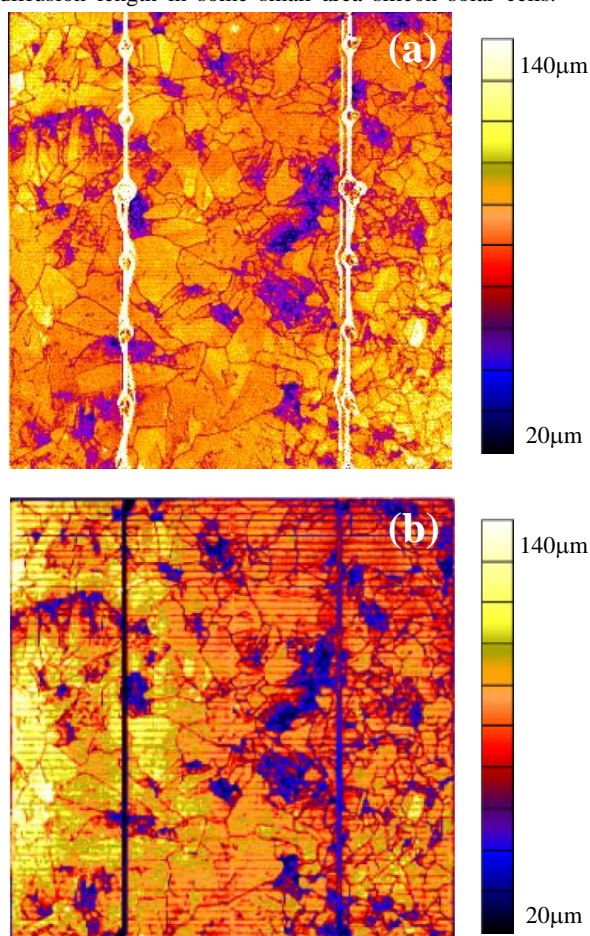


**Figure 5:** Minority carrier diffusion length in  $\mu\text{m}$  measured on a  $10 \times 10 \text{ cm}^2$  screen printed silicon solar cell. (a) from the ratio of two EL images measured with a 1000 nm and a 900 nm short pass filter, respectively, (b) from a spectral LBIC map.

However, this approach ignores the effect of lateral voltage variations across the cell area. These variations are observed in most cells and have a substantial impact on the local EL intensity. They can be caused for example by variations in the local contact resistance or in the emitter sheet resistivity (see e.g. section on series resistance imaging below).

An alternative technique to measure the diffusion length that has recently been introduced and demonstrated is based on calculating the ratio of two EL images measured under identical excitation conditions but with different spectral filters [24]. Fig.5a shows the diffusion length within a  $10 \times 10 \text{ cm}^2$  multicrystalline solar cell obtained using that method.

The diffusion length was obtained from the intensity ratio of two EL images, one measured with a 900 nm short pass filter and the second one with a 1000 nm short pass filter mounted in front of the camera objective. Fig.5b shows the diffusion length distribution as determined from a spectral light beam induced current (LBIC) map measured on the same cell. Both images in Fig.5 are plotted on the same colour scale and excellent quantitative agreement is observed. There are two major advantages of determining the diffusion length from the ratio of two luminescence images compared to the method of using one single EL image. Firstly, intensity variations in single EL images that result from lateral voltage variations are eliminated, which avoids substantial experimental artefacts. Secondly, the intensity ratio provides the absolute diffusion length from two relative luminescence images thereby avoiding the requirement for a separate calibration method. The details of the method and the theory are described in [24] and in [25]. Future work will focus on applying the technique of calculating intensity ratios to the calibration of PL images.

### 4 SERIES RESISTANCE IMAGING

To date the most widely used and established technique to identify local variations in the series resistance in silicon solar cells is Corescan [26]. That technique maps the electrochemical potential in the emitter by scratching a metal probe through the SiN (or SiO<sub>2</sub>) front passivation and antireflection layer, thereby measuring the local electrochemical potential difference between the front grid and the emitter. Using luminescence imaging for spatially resolved measurement of the series resistance was proposed and demonstrated experimentally in Ref.[27]. It was shown that lateral variations of the series resistance show up as variations of the luminescence intensity in EL images and also in PL images that are measured with simultaneous current extraction. A more quantitative determination of spatially resolved series resistance variations from two PL images (PL-Rs), one taken under open circuit conditions and another taken with current extraction, was demonstrated in [28]. The determination of spatially resolved series resistance from a combination of EL imaging with lock-in thermography was demonstrated more recently [29].

In a paper presented at this conference the PL-Rs method for quantitative measurements of the series resistance is demonstrated on multicrystalline solar cells [30]. It is shown that using the approach described in [28]

lateral variations of the minority carrier lifetime are eliminated in the resulting series resistance image. It is also demonstrated experimentally in that paper that PL imaging is sensitive to series resistance effects occurring on both the front and the rear surface in contrast to Corescan, which only measures front surface effects. This aspect is particularly important for cell concepts like laser fired contacts [31] or high efficiency interdigitated rear contact cell concepts [32], in which series resistance effects will occur predominantly on the rear surface.

Fig.6 shows the comparison of the series resistance of a screen printed monocrystalline silicon solar cell determined using the quantitative PL-Rs method presented in [28] with a Corescan measurement taken on the same cell. The PL image shows the series resistance in  $\Omega\text{cm}^2$ , whereas the Corescan presents the local voltage drop between emitter and front grid. The PL-Rs method is advantageous as it provides better spatial resolution

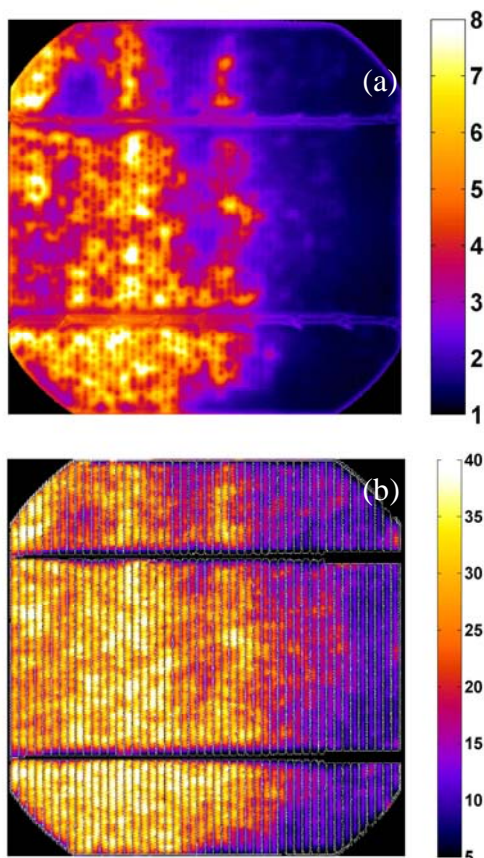


**Figure 6:** Series resistance variation in an industrial 5-inch screen printed monocrystalline silicon solar cell, caused by a non-ideal post-processing anneal. (a) Series resistance in  $\Omega\text{cm}^2$  from photoluminescence imaging, determined from four PL images each measured in 1s, (b) voltage variation between the grid and the emitter measured by CORESCAN using 0.5 mm line spacing and  $30\text{mA}/\text{cm}^2$ . Data acquisition time >40 minutes.

with significantly shorter data acquisition time (total data acquisition time for the PL data was 4s compared to 33 minutes for the Corescan). The data acquisition time required for the PL-Rs method is thus compatible with in-line process monitoring. Another important

consideration that is crucial for in-line applications is that the PL-Rs technique is non-destructive.

## 5 SHUNT IMAGING

The detection of moderate and strong shunts with EL and PL imaging has been demonstrated by various groups (e.g. [33-35]). It has been shown that in both PL and EL images the vicinity of shunted areas appears as a blurred region of reduced luminescence intensity. This blurring is caused by voltage drops associated with lateral current flow through the emitter and through the front surface grid. This is the same effect that causes the blurring in the PL lifetime image shown in Fig.1b.

### 5.1 Numerical modelling of shunts

Two dimensional numerical network modelling was used in Ref.[20] to analyse these blurring effects quantitatively. As an example, Fig.7 shows a simulated photoluminescence intensity distribution from a silicon solar cell with a  $40\ \Omega/\text{sq}$  diffusion and a metal grid on the front surface. The cell has a point like shunt in the middle between two grid fingers. Three images are shown in Fig.7 simulated for different values of the parallel resistance (from left to right  $R_p=640\ \Omega$ ,  $160\ \Omega$  and  $40\ \Omega$ , respectively). The images show how the blurring caused by lateral current flow into the shunts varies with the shunt resistance. A correlation of these theoretical results with experimental luminescence images and a systematic study of luminescence images measured with variable excitation conditions should allow a more quantitative analysis of luminescence images in terms of shunts than currently possible. However, at this stage it cannot be expected that luminescence imaging will be as quantitative as lock-in Thermography methods [36], even when combined with such two dimensional numerical modelling.

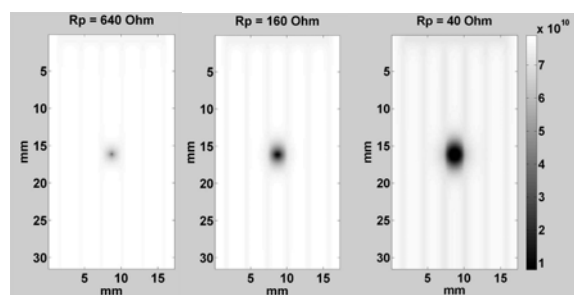


**Figure 7:** Photoluminescence images of the area around a point like shunt in a silicon solar cell simulated using two dimensional network modelling. Increased blurring effects are expected around stronger point like shunts.

### 5.2 Shunt detection and subsequent isolation

A more qualitative shunt localisation from PL/EL images can still be very useful for specific applications. A PL/EL imaging investigation of twenty shunted industrial mc-Si solar cells that were rejected by the manufacturer due to excessive reverse currents and poor electrical performance showed that in most cases the position of the shunt could be identified fairly accurately [37]. As an example Fig.8a shows a PL image taken with one second data acquisition time and with one-Sun

equivalent illumination intensity on a shunted screen printed mc-Si solar cell. The position of the shunt is identified in the vicinity of one finger, the voltage of which is dragged down substantially by the shunt, causing reduced luminescence intensity in the vicinity of the shunt. The inset of Fig.8a shows a section from the same image but plotted on a different colour scale. The position of the shunt (solid arrow) can be readily identified in that representation.

The qualitative shunt localisation from luminescence images followed by shunt isolation was proposed in [34] as a means to reduce the influence of shunts on the average production yield in PV manufacturing. This methodology was demonstrated experimentally in [38] and also at this conference [37]. Once the position of the shunt is known, isolation methods similar to those commonly used for edge isolation in industrial screen printed solar cells can be applied. Fig.8b shows a PL image of the same shunted cell after the shunted region has been electrically isolated from the main part of the cell. The isolation was achieved by using an etching process that removes the silver from the finger on both sides of the shunt. The shunt is confined to a much smaller region after the shunt isolation and no longer contributes significantly to the performance of the cell.

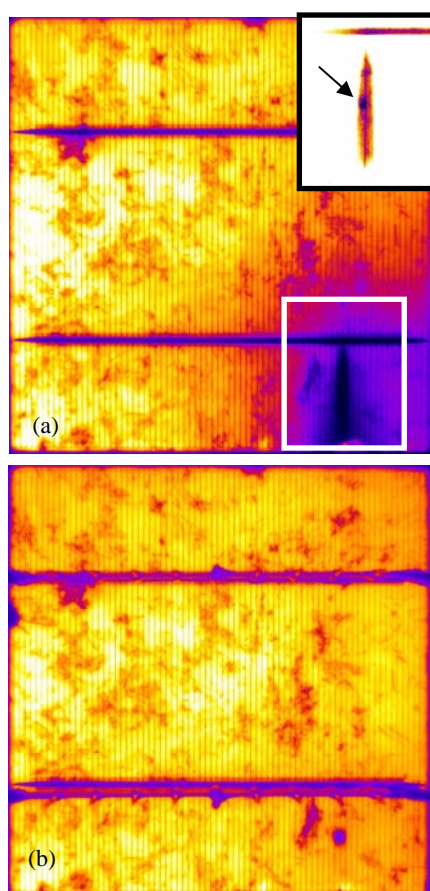


**Figure 8:** PL image of a shunted industrial silicon solar cell measured before (a) and after (b) shunt isolation. See text for details.

At the left hand edge a crack was introduced during cell handling which had no detrimental effect on the cell efficiency.

The isolation of the shunt in this cell resulted in an improvement in the implied fill factor (as determined from Suns-Voc measurements [39]) from 69% to 83% and in cell efficiency under AM1.5 illumination conditions from 13.5% to 15.1%. The lower relative improvement in cell efficiency (11.8%) compared to the relative improvement in implied fill factor (20.3%) is due to series resistance effects that are not measured in Suns-Voc experiments and that start dominating the fill factor once the influence of the shunt resistance is sufficiently suppressed. The excellent fill factors obtained from the Suns-Voc measurements clearly show that after the isolation process the shunt resistance no longer has a significant influence on the cell performance under one-Sun operating conditions. Due to the short data acquisition time of only one second that is required for the PL image, the combination of luminescence imaging and various shunt isolation methods could be a viable approach to reduce the impact of shunted cells on average yield and average efficiency in industrial production.

## 6 IRON IMAGING

Iron is one of the most relevant impurities found in silicon wafers that are used in photovoltaic applications and can be present either in point-like form [40] or as precipitates [41]. The recombination activity of interstitial iron has been found to be more pronounced in p-type silicon [42], which is most commonly used for industrial solar cells. Fast methods that measure the spatially resolved interstitial iron concentration are therefore of interest. Some methods to determine the interstitial iron concentration in boron-doped p-type silicon wafers are based on the fact that the injection level dependent minority carrier lifetime changes dramatically when the chemical state of non-precipitated iron within a silicon sample is changed from FeB pairs to interstitial Fe ( $Fe_i$ ) [43]. The transformation from FeB pairs to  $Fe_i$  can be achieved in practice by continuous strong illumination with a few suns equivalent illumination intensity at room temperature [44] typically for less than one minute.

PL imaging is especially well-suited to iron imaging, due to the speed with which an image can be taken. Both PL images that were used for the iron concentration image shown in Fig.9 were measured with a data acquisition time of only one second each. This short data acquisition time is particularly important for  $Fe_i$ -concentration imaging because it allows the FeB pairs to remain mostly unbroken during the initial measurement, which is essential for accurate determination of the iron concentration. In addition, the second lifetime image can be measured very quickly after the FeB pairs have been dissociated. The influence of the reformation of FeB pairs during the measurement is thus negligible. A more detailed description of the  $Fe_i$ -concentration measurements with photoluminescence imaging can be found in [45].

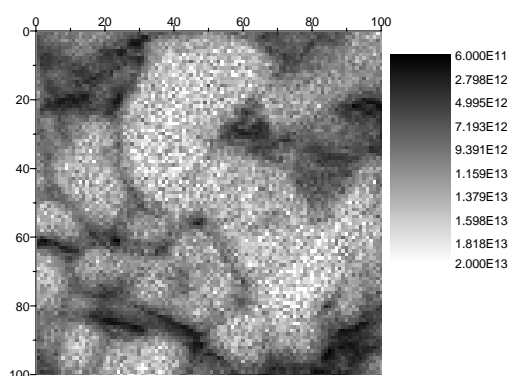


**Figure 9:** Interstitial iron concentration in a  $13 \times 13 \text{ mm}^2$  section of a mc-Si wafer obtained from two PL images (each measured in one second) taken before and after dissociating FeB pairs.

Fig.9 shows the iron concentration in a  $13 \times 13 \text{ mm}^2$  section of a passivated mc-Si wafer as determined from two PL images measured with one-Sun equivalent illumination intensity before and after dissociating the FeB pairs. The dissociation was achieved by intense illumination ( $\sim$ ten-Suns) for one minute. The iron concentration was deduced from the reduction in minority carrier lifetime that is observed upon breaking of FeB pairs at injection levels below the so-called crossover point for Fe/FeB pair dissociation [46]. There is a clear reduction in the interstitial Fe concentration near the grain boundaries and near dislocated regions, indicating internal gettering of iron during crystallization. The average iron concentration in the image is  $9 \times 10^{12} \text{ cm}^{-3}$ , which is similar to the average iron concentration determined across this entire wafer by QSS-PC measurements ( $7 \times 10^{12} \text{ cm}^{-3}$ ).

## 7 DISLOCATION IMAGING

Scientific grade Si CCD cameras were used for all luminescence imaging applications that have been discussed above. These cameras only detect the short wavelength tail of the band-to-band luminescence from silicon samples at room temperature. About an order of magnitude enhancement of the measured photon flux can be achieved by using an InGaAs camera, which is sensitive typically from 900 nm to 1700 nm and thus throughout the entire spectral range in which band-to-band emission from crystalline silicon occurs.

Another benefit of using an InGaAs camera is that it is sensitive to an emission band in the spectral range 1400-1700 nm. The so-called D-band or *defect luminescence* (as it will be referred to here), was first detected in plastically deformed silicon at cryogenic temperatures [47], and is still detectable as a broad featureless spectral emission band around  $\lambda=1550\text{nm}$  at room temperature. The presence of the defect band has been linked to the presence of dislocations, but the exact role of dislocations and of their decoration with specific impurities is not fully understood to date [48]. Scanning photoluminescence *mapping* on mc Si [6] and on string ribbon silicon wafers [49] was used to map the band-to-band and the defect luminescence, respectively. An anti-correlation between the band-to-band luminescence

intensity (which is indicative of the minority carrier lifetime) and the defect luminescence intensity was observed. The intensity ratio of defect band luminescence and band-to-band luminescence was found to be indicative of the local dislocation density.

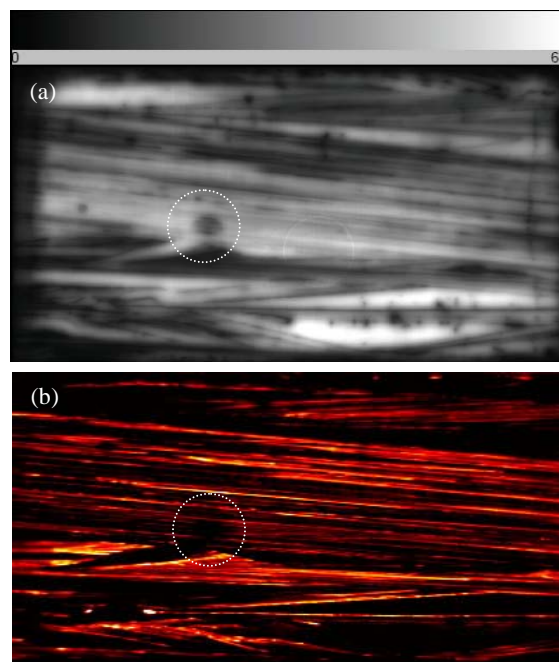


**Figure 10:** String ribbon silicon wafer after emitter diffusion, SiN deposition and firing. (a) Minority carrier lifetime obtained from a band-to-band photoluminescence image measured with a Si-CCD camera. (b) Defect photoluminescence signal measured with an InGaAs camera. See text for details.

Dislocations are structural defects that cannot be removed via gettering and often remain as the efficiency limiting defects at the end of cell processing (see Fig.3). Infrared imaging techniques (ILM [50] / CDI [18]) are affected by minority carrier trapping [51] at low injection levels. The trap density has recently been linked to the dislocation density in measurements on raw wafers and these methods thus appear to have the potential to identify efficiency limiting defects already in the starting material [52, 53]. Here, our aim of imaging the defect luminescence band is similar. That is, we aim to use defect luminescence imaging to identify efficiency limiting dislocation densities early on in the cell process, ideally already in measurements on the starting material, and with data acquisition times that are compatible with measuring every wafer in an in-line process.

Fig.10a shows a calibrated lifetime distribution within a string ribbon wafer after SiN deposition plus firing, obtained from a conventional band-to-band luminescence image taken with a Silicon CCD camera. A defect luminescence image of that wafer was measured at UNSW using a thermoelectrically cooled InGaAs camera with a resolution of  $320 \times 256$  pixels. A dielectric 1300nm long-pass filter in front of the camera was used to block the band-to-band luminescence. The defect luminescence image (Fig.10b) was captured with a data acquisition time of 3s. A clear correlation between low lifetime areas

and high defect luminescence intensity is observed, confirming the results presented in [6]. PL imaging thus allows similar studies but with much shorter measurement times. Fig.10 also shows that dislocation rich regions seem to dominate the cell performance at the end of processing, i.e. after other defects such as point defects and impurities have been either gettered or passivated with hydrogen. Some areas of reduced minority carrier lifetime (e.g. dotted circle in Fig.10) are not caused by dislocations and therefore do not emit long wavelength luminescence. For a quantitative analysis of dislocation densities, the PL signal in the defect band must therefore be normalised against the band-to-band PL signal as proposed in [6].

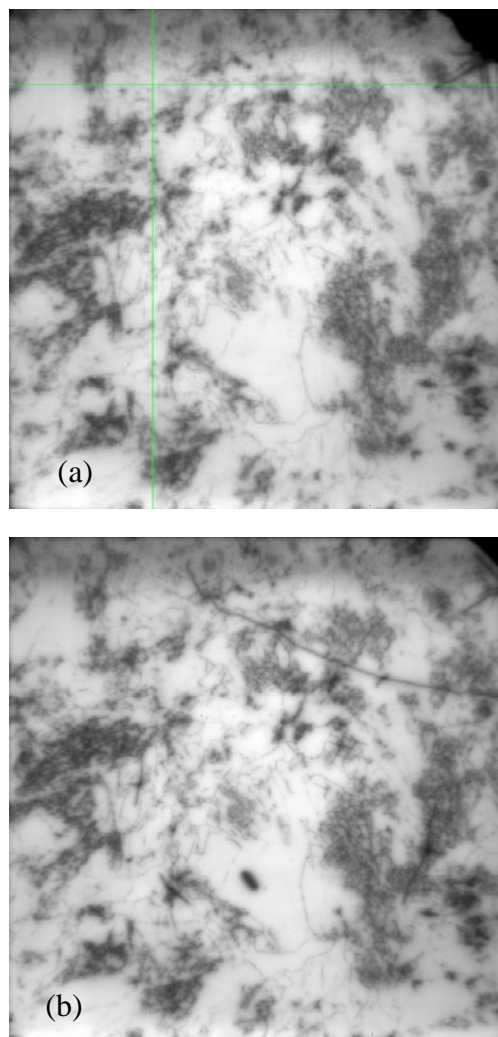
Measurements on a number of dislocation rich string ribbon silicon samples at various processing stages showed that prior to SiN firing the defect luminescence signal is too weak to yield acceptable signal to noise ratios with data acquisition times of <10 s and with illumination intensities of <ten-Suns. For example no detectable defect luminescence signal was observed even with ten-Suns equivalent illumination intensity on unprocessed string ribbon and mc-Si wafers. PL imaging of the defect band at room temperature on silicon wafers thus does not appear to be a practical alternative to band-to-band PL imaging or ILM/CDI for fast (i.e. in-line) characterisation of silicon wafers at an early stage of processing.

## 8 CRACK DETECTION

Wafer and cell breakage causes major yield losses in industrial manufacturing of solar cells and PV modules. Techniques that are under development for crack detection include Resonance Ultrasonic Vibration (RUV) [54-56], Radiant Heating/Thermography (RHT) [57] and Ultrasonic Thermography (UT) [58]. A commercial prototype of an in-line RUV tool has recently been developed [59].

The detection of cracks in silicon solar cells by EL imaging (see e.g. [60, 61]) and in silicon wafers by PL imaging (e.g. [2, 27]) has been demonstrated previously. PL imaging is particularly appealing for crack detection as it is a fast and non-contact technique that can be applied before and after any processing stage. Distinguishing cracks from other recombination active regions such as dislocation networks or grain boundaries is not a trivial task, particularly in mc-Si wafers (see Fig.11). The variety of features that are typically observed in PL images taken on mc-Si samples makes identifying cracks with lengths on the order of only a few mm or even centimetres unreliable if only one single image is inspected.

An approach presented at this conference to enhance the sensitivity and reliability of PL imaging for crack detection in mc-si wafers is to compare PL images taken under identical conditions on sister wafers, i.e. neighbouring wafers cut from the same ingot [62]. The idea is that material induced defects such as dislocations and grain boundaries cause surprisingly similar features in PL images measured on adjacent wafers. On the other hand cracks are often either introduced or significantly expanded during processing and are therefore unlikely to have the exact same shape and be present in the same location in adjacent wafers.



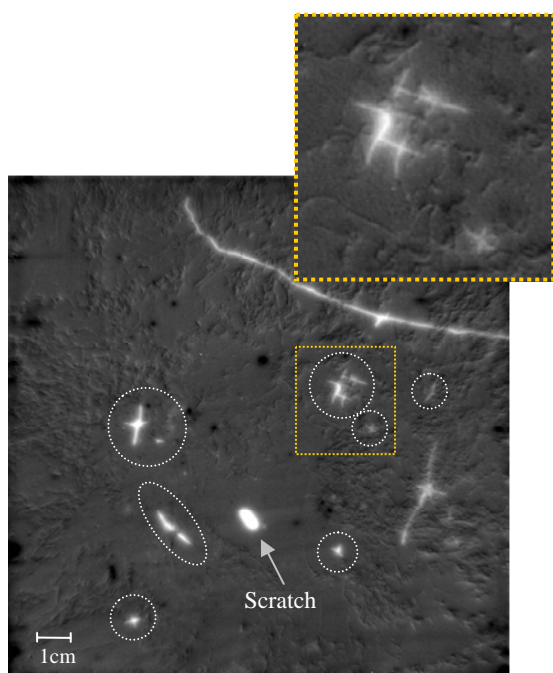
**Figure 11:** PL images measured with one-Sun equivalent illumination intensity on two mc-Si sister wafers after emitter diffusion and SiN deposition. One wafer (a) was measured as received, the second wafer (b) was processed as described in the text.

Fig.11 shows PL images of two mc-Si sister wafers measured after diffusion and SiN deposition. Both wafers have cracks and a piece broken off at the top edge, which was introduced during manual handling of the wafers. Several small and large cracks were intentionally introduced into the second wafer (Fig.11b). In addition a scratch (~7mm) was introduced using a diamond pen. Except for the large extended and almost horizontal crack at the top of the wafer it is difficult to identify any features in Fig.11b unambiguously as cracks. The direct comparison of the two images in Fig.11 already gives some better idea, which features are grown in defects and which were introduced.

Fig.12 shows the normalised intensity difference between the two images, a representation in which identical intensities result in a value of 0.5 and the difference in intensity ranges from zero to unity. Several cracks of variable length clearly show up as pronounced features. The smallest cracks (inset of Fig.12) that are visible in the intensity difference are only ~4mm in size. The “star-

shape” of this defect allows identifying this defect as a crack with high certainty. The diamond pen scratch (arrow) for instance has caused junction shunting, which is associated with blurring effects and which is clearly distinct from the cracks. More statistical analysis is required to identify how accurately and reliably cracks can be distinguished from scratches using this method.

In highly automated production lines, in which wafers from the same ingot can be processed in a systematic way [63] this method could be extremely valuable in gathering statistical data about cracks that are introduced or expanded during processing, eventually resulting in algorithms to sort out cracked wafers.



**Figure 12:** Normalised Intensity Difference (see text for details) of the two images shown in Fig.11. Cracks that were introduced in one wafer and a scratch with a diamond pen are clearly identified.

## 9 SUMMARY AND CONCLUSIONS

This paper reviews the exceptional variety of material and cell parameters that can be measured on silicon wafers and silicon solar cells with high lateral spatial resolution using luminescence imaging techniques. Luminescence imaging is easy to use, can be measured at room temperature, requires no specific sample preparation, can be measured on planar and textured samples of any size and at any processing stage and is free from artefacts resulting from minority carrier trapping or caused by carriers stored in space charge regions. Quantitative information can be obtained from luminescence imaging about the minority carrier lifetime, the diffusion length, the series resistance, the position of cracks and the iron concentration (the latter in boron-doped p-type wafers). Very valuable information about the shunt resistance or dislocation densities can also be obtained from luminescence imaging, in some cases in a somewhat more qualitative fashion. This versatility combined with extremely short data acquisition times

makes luminescence imaging techniques very attractive for in-line monitoring in industrial applications.

The next step in the development of PL/EL imaging is to demonstrate how the vast amount of spatially resolved information (available in principle on every wafer or solar cell in a production) can be used to make better solar cells with higher average production yield. To this end, a systematic PL imaging study of a large number of wafers before and after key processing stages is required. A statistical analysis will then provide algorithms that allow optimisation of the production e.g. adjusting process parameters based on individual PL images or sorting out low quality or cracked wafers. This procedure will assist in establishing luminescence imaging into a standard in-line process monitoring tool that should be part of every production line in the future.

**Acknowledgement** The Centre of Excellence for Advanced Silicon Photovoltaics and Photonics is supported under the Australian Research Council's Centres of Excellence Scheme.

## REFERENCES

1. T. Fuyuki, H. Kondo, T. Yamazaki, Y. Takahashi, and Y. Uraoka, *Applied Physics Letters* **86**(26) (2005) 262108.
2. T. Trupke, R.A. Bardos, M.C. Schubert, and W. Warta, *Applied Physics Letters* **89** (2006) 044107.
3. T. Trupke, J. Zhao, A. Wang, R. Corkish, and M.A. Green, *Applied Physics Letters* **82**(18) (2003) 2996-2998.
4. M.A. Green, J. Zhao, A. Wang, P.J. Reece, and M. Gal, *Nature* **412**(6849) (2001) 805-808.
5. T. Trupke and R.A. Bardos, 31st IEEE PVSC, Orlando, USA (2005).
6. S. Ostapenko, I. Tarasov, J.P. Kalejs, C. Haessler, and E.U. Reisner, *Semiconductor Science and Technology* **15**(8) (2000) 840-848.
7. S. Ostapenko, I. Tarasov, S. Lulu, A. Belyaev, and M. Dybiec, NCPV and Solar Program Review Meeting, NREL/CD-520-33586 (2003) 231.
8. E. Daub, P. Klopp, S. Kugler, and P. Würfel, 12th EPVSC, Amsterdam, 1994.
9. P. Würfel, *Physics of solar cells*. 2005: Wiley-VCH Verlag GmbH & Co. KGaA, Weinheim.
10. P. Würfel, *Journal of Physics C: Solid State Physics* **15**(18) (1982) 3967-85.
11. G. Smestad and H. Ries, *Solar Energy Materials and Solar Cells* **25** (1992) 51-71.
12. G. Smestad, PhD thesis, EPFL, Lausanne, Switzerland (1994).
13. R.A. Bardos, T. Trupke, M.C. Schubert, and T. Roth, *Applied Physics Letters* **88** (2006) 053504.
14. P.J. Cousins, D.H. Neuhaus, and J.E. Cotter, *Journal of Applied Physics* **95**(4) (2004) 1854-1858.
15. M. Bail, M. Schulz, and R. Brendel, *Applied Physics Letters* **82**(5) (2003) 757-759.
16. T. Trupke, *Journal of Applied Physics* **100**(6) (2006) 063531.
17. R.A. Sinton, A. Cuevas, and M. Stuckings, 25th IEEE PVSC, Washington, USA (1996).
18. S. Riepe, J. Isenberg, C. Ballif, S.W. Glunz, and W. Warta, 17th EPVSC, Munich (2001).

19. J.C. Goldschmidt, O. Schultz, and S.W. Glunz, Proceedings of the 20th EPVSC, Barcelona, Spain, 2005 663.
20. M. Kasemann, D. Grote, B. Walter, T. Trupke, Y. Augarten, R.A. Bardos, E. Pink, M.D. Abbott, and W. Warta, this conference.
21. E. Yablonovitch, D.L. Allara, C.C. Chang, T. Gmitter, and T.B. Bright, Physical Review Letters **57**(2) (1986) 249.
22. H. Sugimoto and M. Tajima, Japanese Journal of Applied Physics **46**(15) (2007) L339.
23. M. Tajima, 17th Crystalline Silicon Workshop, Vail, USA, August (2007).
24. P. Würfel, T. Trupke, T. Puzzer, E. Schäffer, W. Warta, and S. Glunz, Journal of Applied Physics **101** (2007) 123110.
25. P. Würfel, T. Trupke, M. Rüdiger, E. Schäffer, T. Puzzer, W. Warta, and S.W. Glunz, this conference.
26. A.S.H.v.d. Heide, A. Schoenecker, G.P. Wyers, and W.C. Sinke, 16th EPVSC, Glasgow, UK (2000).
27. T. Trupke, R.A. Bardos, M.D. Abbott, F.W. Chen, J.E. Cotter, and A. Lorenz, WCPEC-4, Waikoloa, USA (2006).
28. T. Trupke, E. Pink, R.A. Bardos, and M.D. Abbott, Appl. Phys. Lett. **90** (2007) 093506.
29. K. Ramspeck, K. Bothe, D. Hinken, B. Fischer, J. Schmidt, and R. Brendel, Applied Physics Letters **90**(15) (2007) 153502.
30. E. Pink, S. Kontermann, T. Trupke, R.A. Bardos, M.D. Abbott, and Y. Augarten, this conference.
31. E. Schneiderlöchner, R. Preu, R. Lüdemann, and S.W. Glunz, Progress in Photovoltaics **10**(1) (2002) 29-34.
32. M.D. Lammert and R.J. Schwartz, IEEE Transactions on Electron Devices **24**(4) (1977) 337.
33. K. Bothe, P. Pohl, J. Schmidt, T. Weber, P.P. Altermatt, B. Fischer, and R. Brendel, 21st European Photovoltaic Solar Energy Conference, Dresden, Germany (2006) 597.
34. T. Trupke, R.A. Bardos, M.D. Abbott, K. Fisher, J. Bauer, and O. Breitenstein, International Workshop on Science and Technology of Crystalline Silicon Solar Cells, Sendai, Japan, 2-3 October (2006).
35. M. Kasemann, M.C. Schubert, M. The, M. Köber, M. Hermle, and W. Warta, Applied Physics Letters **89** (2006) 224102.
36. O. Breitenstein and M. Langenkamp, *Lock-In Thermography - Basics and use for functional diagnostics of electronic components*. 2003, Heidelberg: Springer.
37. Y. Augarten, M.D. Abbott, T. Trupke, R.A. Bardos, H.P. Hartmann, R. Gupta, and O. Breitenstein, this conference.
38. M.D. Abbott, T. Trupke, H.P. Hartmann, R. Gupta, and O. Breitenstein, Progress in Photovoltaics (2007) in press.
39. R.A. Sinton and A. Cuevas, 16th EPVSC, Glasgow, United Kingdom (2000) 1152.
40. R.A. Sinton, T. Mankad, S. Bowden, and N. Enjalbert, Proceedings 19th European Photovoltaic Solar Energy Conference (2004) 520-523.
41. T. Buonassisi, A.A. Istratov, M. Heuer, M.A. Marcus, R. Jonczyk, J. Isenberg, B. Lai, Z. Cai, S. Heald, W. Warta, R. Schindler, G. Willeke, and E.R. Weber, Journal of Applied Physics **97** (2005) 074901.
42. D. Macdonald and L.J. Geerligs, Applied Physics Letters **85**(18) (2004) 4061-4063.
43. J.E. Birkholz, K. Bothe, D. Macdonald, and J. Schmidt, Journal of Applied Physics **97** (2005) 103708.
44. G. Zoth and W. Bergholz, Journal of Applied Physics **67**(11) (1990) 6764-6771.
45. D. Macdonald, J. Tan, R.A. Bardos, and T. Trupke, this conference.
46. D. Macdonald, L.J. Geerligs, and A. Azzizi, Journal of Applied Physics **95**(3) (2004) 1021-1028.
47. N.A. Drozdov, A.A. Patrin, and V.D. Tkachev, Physica Status Solidi B: Basic Research **83**(2) (1977) K137-K139.
48. T. Arguirov, W. Seifert, M. Kittler, and J. Reif, Journal of Physics: Condensed Matter **14**(48) (2002) 13169-13177.
49. I. Tarasov, S. Ostapenko, K. Nakayashiki, and A. Rohatgi, Applied Physics Letters **85**(19) (2004) 4346-4348.
50. M. Bail, J. Kentsch, R. Brendel, and M. Schulz, 28th IEEE PVSC, Anchorage (2000).
51. P. Pohl, J. Schmidt, K. Bothe, and R. Brendel, Applied Physics Letters **87**(14) (2005) 142104.
52. M.C. Schubert and W. Warta, Progress in Photovoltaics **15**(4) (2007) 331-336.
53. P. Pohl, J. Schmidt, C. Schmiga, and R. Brendel, Journal of Applied Physics **101**(7) (2007) 073701.
54. S. Ostapenko, W. Dallas, D. Hess, O. Polupan, and J. Wohlgemuth, WCPEC-4, Hawaii, USA, May (2006).
55. W. Dallas, O. Polupan, and S. Ostapenko, Measurement Science and Technology **18**(3) (2007) 852-858.
56. A. Belyaev, O. Polupan, W. Dallas, S. Ostapenko, D. Hess, and J. Wohlgemuth, Applied Physics Letters **88**(11) (2006) 111907/1-111907/3.
57. J.M. Murach, M.J. Nowlan, S.F. Sutherland, D.C. Miller, S.B. Moore, and S.J. Hogan, Annual Technical Progress Report, 1 January 2003 – 30 June 2004, Spire Corporation, Bedford, Massachusetts, USA.
58. O.B. J. P. Rakotoniaina, M. H. Al Rifai, D. Franke, A. Schneider, Proceedings of the 19th Europ. Photovoltaic Solar Energy Conference and Exhibition, Paris 7-11 June 2004 (2004) 640-643.
59. [www.ultrasonictech.com](http://www.ultrasonictech.com).
60. Y. Takahashi, Y. Kaji, O. Ogane, Y. Uruoka, and T. Fuyuki, WCPEC-4, Hawaii, USA, May (2006) 924.
61. A.M. Gabor, M. Ralli, S. Montminy, I. Alegria, C. Bordonaro, J. Woods, L. Felton, M. Davis, B. Atchley, and T. Williams, 21st European Photovoltaic Solar Energy Conference, Dresden, Germany (2006) 2042.
62. R.A. Bardos and T. Trupke, this conference.
63. S. Rein, A. Krieg, A.W. Weil, A. Grohe, D. Biro, and R. Preu, this conference.